Extended Tersoff potential for boron nitride: Energetics and elastic properties of pristine and defective h -BN

J. Los, M. Kroes, K. Albe, M. Gordillo, M. I. Katsnelson, A. Fasolino

Extended Tersoff potential for boron nitride: Energetics and elastic properties of pristine and defective *h*-BN

J. H. Los,[1,*] J. M. H. Kroes,[1] K. Albe,[2] R. M. Gordillo,[3] M. I. Katsnelson,[1] and A. Fasolino[1]

[1]*Radboud University, Institute for Molecules and Materials, Heyendaalseweg 135, 6525AJ Nijmegen, The Netherlands*

[2]*Technische Universität Darmstadt, Institut für Materialwissenschaft, Fachgebiet Materialmodellierung, Jovanka-Bontschits-Str. 2, D-64287 Darmstadt, Germany*

[3]*Aix-Marseille Université and CNRS, CINaM UMR 7325, 13288 Marseille, France*

(Received 24 May 2017; revised manuscript received 23 October 2017; published 20 November 2017)

We present an extended Tersoff potential for boron nitride (BN-ExTeP) for application in large scale atomistic simulations. BN-ExTeP accurately describes the main low energy B, N, and BN structures and yields quantitatively correct trends in the bonding as a function of coordination. The proposed extension of the bond order, added to improve the dependence of bonding on the chemical environment, leads to an accurate description of point defects in hexagonal BN (*h*-BN) and cubic BN (*c*-BN). We have implemented this potential in the molecular dynamics LAMMPS code and used it to determine some basic properties of pristine 2D *h*-BN and the elastic properties of defective *h*-BN as a function of defect density at zero temperature. Our results show that there is a strong correlation between the size of the static corrugation induced by the defects and the weakening of the in-plane elastic moduli.

DOI: 10.1103/PhysRevB.96.184108

I. INTRODUCTION

Following the discovery of graphene, many other 2D materials have been identified [1]. Of these, monolayer hexagonal boron nitride (*h*-BN) is attracting increasing attention as a prototype substrate for graphene thanks to its similar structure, chemical inertness, and the insulating character [2,3]. The large 5–6 eV band gap [4] makes *h*-BN transparent, whence its nickname "white graphene," and makes it suitable for application in deep UV optoelectronic devices [5,6].

Besides *h*-BN, BN and the pure components B and N exist in many competing phases. Different classical potentials have been parametrized for B-N systems, including a number of Tersoff potentials [7–10]. For *h*-BN, Kınacı *et al.* parametrized a Tersoff potential to describe phonons and thermal transport [9,10] while Matsunaga *et al.* parametrized a Tersoff potential to study cubic boron carbonitrides [8]. Also several ReaxFF potentials have been parametrized to describe liquids with molecules including boron and nitrogen [11,12]. Of the existing potentials for BN proposed thus far, however, none are meant to describe the larger class of solid phases of B, N, and BN, as well as various defects that typically occur in CVD grown and irradiated materials [13–15].

Here we introduce BN-ExTeP, an extended Tersoff potential for BN specifically aimed at describing correctly the dependence on coordination and chemical environment of the bonding occurring in B, N, and B-N systems. The normal Tersoff part of the potential improves an earlier Tersoff potential by Albe and Möller for BN [7,16]. For the here presented potential, special attention is paid to achieving an optimal description of 2D *h*-BN, including its thermal stability, lattice parameter, and elastic properties. Regarding its elastic properties, it solves the artifact of the earlier potential [7,16] that yields a too large uniaxial modulus and a negative Poisson's ratio, in disagreement with *ab initio* calculations [17,18]. In addition, BN-ExTeP yields a lattice parameter for *h*-BN in perfect agreement with the experimental value, which makes it, in conjunction with a potential for carbon, particularly suitable for application to graphene/*h*-BN heterostructures requiring an accurate description of the lattice mismatch between graphene and *h*-BN. To improve the description of nonpristine structures, in particular defected *h*-BN and *c*-BN, a correction to the bond order is introduced that explicitly takes into account the chemical environments of the atoms involved in the bond, as suggested in Ref. [16]. While the pure B parametrization in BN-ExTeP is practically the same as in Ref. [16], the parametrization of the pure N part has been modified to improve the binding energies of the relatively stable pure N 2D honeycomb and diamond lattices and the BN interactions have been reparametrized to improve the description of *h*-BN and *c*-BN.

The complete BN-ExTeP has been implemented in LAMMPS [19] and allows for large scale molecular dynamics simulations of BN systems. Here, we use it to study the elastic properties of defective *h*-BN at $T = 0$ K as a function of defect density. For *h*-BN with randomly distributed defects we find a weakening of the elastic constants with increasing defect density that is much more pronounced for those defects that induce large static corrugations of the layer.

In Sec. II we give a brief description of the potential, for which we provide the numerical parametrization in Sec. III. In Sec. III A we present the parametrization of the Tersoff potential, optimized for the description of reference B, N, and BN molecular and crystal structures not involving the correction term. In Sec. III B, we then compare the structure and energetics of many point defects in *h*-BN and *c*-BN and of binary molecular structures to *ab initio* results to complete the parametrization of the correction term. Our results from large scale simulations of pristine and defective 2D *h*-BN will be presented in Secs. IV and V, respectively. Conclusions and perspectives are given in Sec. VI.

*j.los@science.ru.nl

II. DESCRIPTION OF THE POTENTIAL

BN-ExTeP extends the classical Tersoff potential [20] with a correction to the bond order that allows us in particular to discriminate bonding situations where the coordination numbers are identical but chemical identities are not. For completeness, the description below also includes the basic form of the Tersoff potential [20].

The total binding energy of the system is given by

$$E = \frac{1}{2}\sum_{i,j} f_C(r_{ij})[V_R(r_{ij}) - B_{ij}V_A(r_{ij})]. \tag{1}$$

The double sum here runs over all atoms i and j, and f_C is a smooth cutoff function:

$$f_C(r) = \begin{cases} 1 & r \leqslant R - D \\ \frac{1}{2}\left[1 - \sin\left(\frac{\pi(r-R)}{2D}\right)\right] & |R - r| < D \\ 0 & r \geqslant R + D \end{cases}. \tag{2}$$

V_R and V_A are the repulsive and attractive potentials, respectively,

$$V_R(r) = \frac{D_0}{S-1}\exp\left[-\beta\sqrt{2S}(r - r_0)\right], \tag{3}$$

$$V_A(r) = \frac{SD_0}{S-1}\exp\left[-\beta\sqrt{2/S}(r - r_0)\right], \tag{4}$$

so that the dimer bond energy, $V_R(r) - V_A(r)$, has a minimum at $r = r_0$ equal to $-D_0$. B_{ij} is the total bond order,

$$B_{ij} = \tfrac{1}{2}(b_{ij} + b_{ji}) + F_{ij}, \tag{5}$$

where b_{ij} is the usual Tersoff bond order and F_{ij} is the proposed correction.

The Tersoff bond order b_{ij} is a many-body term involving the relative positions of nearest neighbors reading

$$b_{ij} = \left(1 + \gamma^n \chi_{ij}^n\right)^{-1/(2n)}, \tag{6}$$

where

$$\chi_{ij} = \sum_{k\neq i,j} f_C(r_{ik})g(\theta_{ijk})\exp\left(\lambda_3^3(r_{ij} - r_{ik})^3\right), \tag{7}$$

with θ_{ijk} the angle between $\mathbf{r}_{ij}$ and $\mathbf{r}_{ik}$ and

$$g(\theta) = 1 + \frac{c^2}{d^2} - \frac{c^2}{d^2 + (h - \cos\theta)^2}. \tag{8}$$

The correction term reads

$$F_{ij} = F_{\text{env}}(N_{ij}, N_{ji})F_{IJ}\left(N_{ij}^{\bar{I}}, N_{ji}^{\bar{J}}\right), \tag{9}$$

where F_{env} is an envelope function that smoothly switches off the correction term for the BN dimer and for high (total) coordinations N_{ij} and/or N_{ji}, and where $F_{IJ}(N_{ij}^{\bar{I}}, N_{ji}^{\bar{J}})$ is the correction term proposed in Ref. [16], which depends on the partial, reduced coordination numbers $N_{ij}^{\bar{I}}$ and $N_{ji}^{\bar{J}}$ for neighbors with a chemical identity $\bar{I}$ and $\bar{J}$ other than the identity I of atom i and J of atom j, respectively, with I, J = B,N. The total, reduced coordination N_{ij}, excluding neighbor j, is given by:

$$N_{ij} = \sum_{k\neq i,j} f_C(r_{ik}), \tag{10}$$

whereas the partial, reduced coordination $N_{ij}^{\bar{I}}$ is given by:

$$N_{ij}^{\bar{I}} = \sum_{k\neq i,j} f_C(r_{ik})\delta_{\bar{I},K}, \tag{11}$$

where $\delta_{\bar{I},K}$ is one if the chemical identity K of atom k is not equal to the chemical identity I of atom i and zero otherwise. The envelope function reads:

$$F_{\text{env}}(N_{ij}, N_{ji}) = F_{\text{env},0}(N_{ij}, N_{ji})F_{\text{env},4}(N_{ij})F_{\text{env},4}(N_{ji}) \tag{12}$$

with:

$$F_{\text{env},0}(x, y) = 1 - (1 - x)^2(1 - y)^2 \tag{13}$$

for $x, y < 1$ and $F_{\text{env},0}(x, y) = 1$ otherwise, and

$$F_{\text{env},4}(x) = (2x - 5)(4 - x)^2 \tag{14}$$

for $3 < x < 4$, while $F_{\text{env},4}(x) = 1$ for $x \leqslant 3$ and $F_{\text{env},4}(x) = 0$ for $x \geqslant 4$. This envelope guarantees continuity up to first order derivatives as required for molecular dynamics simulation.

The low energy structures in BN systems are low coordinated ($\leqslant$4) and accordingly the correction term parameters F_{IJ} are fitted to low coordination configurations. The envelope function in Eq. (9) is applied to avoid unphysical stabilization of configurations with high coordination (>4) due to correction terms. Without F_{env} we found unphysical, relatively high coordinated configurations appearing during melting of c-BN or h-BN.

For noninteger arguments, F_{IJ} is evaluated using a spline, identical to that used for the conjugation term in LCBOP [21], based on the values F_{IJ} and the first order partial derivatives of F_{IJ} at the integer, grid points $(N_{ij}^{\bar{I}}, N_{ji}^{\bar{J}})$ for $0 \leqslant N_{ij}^{\bar{I}} \leqslant 4$ and $0 \leqslant N_{ji}^{\bar{J}} \leqslant 4$. The values of F_{IJ} for $N_{ij}^{\bar{I}} = 4$ and/or $N_{ji}^{\bar{J}} = 4$ are set equal to $F_{IJ}(4, N_{ji}^{\bar{J}}) = F_{IJ}(3, N_{ji}^{\bar{J}})$ and $F_{IJ}(N_{ij}^{\bar{I}}, 4) = F_{IJ}(N_{ij}^{\bar{I}}, 3)$. Partial derivatives with respect to $N_{ij}^{\bar{I}}$ are set to zero at grid points with $N_{ji}^{\bar{J}} = 0$, 3 and 4, and partial derivatives with respect to $N_{ji}^{\bar{J}}$ are set to zero at grid points with $N_{ij}^{\bar{I}} = 0$, 3, and 4. In the other cases, the partial derivative at a given grid point is also set to zero if the values of F_{ij} at the two neighboring grid points are both smaller or both larger than the value of F_{ij} at the given grid point. In the remaining cases, the partial derivatives are computed by a centered, finite difference expression based on the values at these neighboring grid points, e.g., $\partial F_{ij}/\partial N_{ij}^{\bar{I}} = (F_{ij}(N_{ij}^{\bar{I}} + 1, N_{ji}^{\bar{J}}) - F_{ij}(N_{ij}^{\bar{I}} - 1, N_{ji}^{\bar{J}}))/2$ at the grid point $(N_{ij}^{\bar{I}}, N_{ji}^{\bar{J}})$.

III. PARAMETRIZATION

A. Tersoff potential

We first parametrize the Tersoff part of BN-ExTeP by least square fitting to reference values for B, N, and BN structures with variable coordination environments. Most of the reference values were obtained from *ab initio* calculations within density functional theory (DFT) using the DMol code and reported in Ref. [16]. Where available, these values were compared to experimental data or other *ab initio* values from the literature. For all defects in h-BN apart from the intercalation defects (see Tables V and VI), we also performed DFT calculations

TABLE I. Tersoff potential parameters for BN systems. The parameters for BB were taken from Ref. [16], except for λ_3. For NN, part the parameters were adopted from Refs. [7,16], but n, γ, c, d, and h where refitted in this work. The BN part was completely refitted in the present work.

	BB	NN	BN
D_0 (eV)	3.08	9.91	6.36
r_0 (Å)	1.59	1.11	1.3253868267
β (Å^{-1})	1.84	1.92787	1.9931611199
S	1.065264	1.0769	1.0952902519
n	1.142247	0.665	0.6576543657
γ	0.01498959	0.019251	0.0027024851
c	26617.3	23.5	306.586555205
d	141.2	3.75	10.0
h	−0.13	−0.4	−0.7218
λ_3 (Å^{-1})	0	0	0
R (Å)	2.0	2.0	2.0
D (Å)	0.2	0.2	0.2

using the SIESTA code [22]. These DFT calculations were done using the Perdew-Burke-Ernzerhof (PBE) parametrization of the generalized gradient approximation [23] for the exchange-correlation functional. We used norm-conserving Troullier-Martin pseudopotentials [24] and a numerical atomic orbital with double-ζ plus polarization basis set to represent the valence electrons with a real-space integration grid of 300 Ry. Periodic boundary conditions were applied to a supercell of 43.23×44.94 Å, consisting of 720 atoms for pristine h-BN, and a 4×4 k-point sampling was used.

The parametrization of the Tersoff part of BN-ExTeP is given in Table I. The parameters for pure B, except for λ_3, and part for the parameters for pure N were taken from Refs. [16]. A summary of the properties of pure B and N reference structures and of the BN compound structures h-BN and c-BN is given in Tables II and III, respectively.

Table II reveals that, for B, the most stable low temperature structures are those with intermediate coordinations, like the icosahedral cluster with fivefold coordinated atoms and the related α-boron crystal structure containing sixfold and sevenfold coordinated atoms. The latter structure is a polymorph made of a close packing of chemically interconnected icosahedra. The most stable crystalline phase of B at ambient conditions is, however, the β-polymorph, a much more complex structure which can be described as an icosahedral central unit, icosahedrally surrounded by other icosahedra, with a rhombohedral unit cell containing 105 atoms. Obviously, one cannot expect, nor is it the aim here, to describe such structures with high accuracy with a simple Tersoff potential. Therefore, for convenience only the α phase was used as a reference in the fitting procedure, which is enough for obtaining the correct quantitative trends in the coordination dependence of the binding energy per atom. We note that the α and β phase have rather similar structures, both being made of icosahedral units, with the β phase being more stable by only about 0.1 eV/atom [25]. The underestimation of the lattice parameter of the FCC structure is due to the choice of the cutoff range applied, which is suitable for relatively stable structures but not for the FCC lattice.

TABLE II. Ground state equilibrium nearest neighbor distances $r_{eq,0}$ and binding energies per atom E_b for pure B (upper table) and N (lower table) reference structures according to BN-ExTeP, compared to references values (in parenthesis) mostly obtained from *ab initio* calculations [16,26]. For α-boron, experimental data are used [28,29]. Reference values in square brackets were not used in the fitting procedure.

Boron structures	$r_{eq,0}$ (Å)	E_b (eV/atom)
dimer	1.59 (1.59)	1.540 (1.540)
B_3 (triangle)	1.63 (1.58)	2.770 (3.110)
B_3 (linear)	1.62 [1.52]	1.900 [2.486]
B_4 (rhombus)	1.64 [1.54]	3.250 [3.723]
B_{12} (icosahedron)	1.74 (1.72)	5.125 (5.250)
α-boron	1.80 ±0.03 (1.77 ±0.2)	5.650 (5.810)
FCC	1.94 (1.21)	5.332 (5.700)
Nitrogen structures	$r_{eq,0}$ (Å)	E_b (eV/atom)
dimer	1.110 (1.11)	4.955 (4.955)
N_3 (linear)	1.307 (1.21)	3.788 (3.653)
N_3 (triangle)	1.645	2.179
honeycomb hexagonal	1.521 (1.51)	4.647 (4.560)
diamond	1.635 (1.79)	4.494 (4.240)
simple cubic	1.943 (2.00)	2.447 (3.480)
FCC	2.054 (1.39)	1.638 (3.060)

Unlike B, N prefers low coordination with the dimer as the energetically most stable structure, as correctly reproduced by the Tersoff potential. For N, also the energies of the low coordinated honeycomb and diamond lattices are quite well described, while the higher coordinated simple cubic and

TABLE III. Overview of ground state properties of h-BN and c-BN, compared to those from *ab initio* calculations and experimental data. Binding energies E_b are given in eV per BN chemical unit (c.u.). The 2D shear modulus μ_{2D}, Young's modulus E_{2D}, and Poisson's ratio ν_{2D} were determined from B_{2D} and $C_{11,2D}$ using Eq. (15). Elastic constants were calculated including relaxation, except for C_{44}^0, the adiabatic shear elastic constant for c-BN.

***h*-BN**	BN-ExTeP	*ab initio*	Experiment
a (Å)	2.504	2.496	2.504 [30,31]
$c_\perp$ (Å)		6.490	6.66 [30–32]
E_b (eV/c.u.)	−13.38	−12.826	−13.322 [35]
B (GPa)		30.1, 26 [33]	36.7 [30],25.6 [32]
B_{2D} (N/m)	164	164 [33], 280 [34]	
$C_{11,2D}$ (N/m)	277	293 [34]	
μ_{2D} (N/m)	113	114 [34]	
E_{2D} (N/m)	267	278 [34]	
ν_{2D} (N/m)	0.186	0.225 [34], 0.2 [17]	
***c*-BN**			
a (Å)	3.5575	3.593	3.615 [36,37]
E_b (eV/c.u.)	−13.49	−12.94	−13.49 [35]
B (GPa)	402	395	369–400 [37,38]
C_{11} (GPa)	638	803	820 [38]
C_{44} (GPa)		475	480 [38]
C_{44}^0 (GPa)	553	591	

FCC lattices are sufficiently higher in energy to make these structures safely unstable. In the DMol *ab initio* calculations, the N_3 triangular cluster could not be geometrically optimized due to instability, but in Ref. [26], this cluster was found to be 1.37 eV/atom less stable than linear N_3, which is roughly reproduced by our potential.

Table III shows the comparison for the BN compound structures. Almost all reference properties, including the elastic moduli, are rather well reproduced by BN-ExTeP, with c-BN correctly described as the most stable BN polymorph at the given stoichiometry.

The parametrization was performed such that the (in-plane) lattice parameter for h-BN exactly matches the experimental value, a property which is desirable for studying heterostructures made of h-BN and graphene with the correct lattice mismatch between the two materials, required, e.g., for an accurate description of moiré pattern formation [27]. Note that in LAMMPS, BN-ExTeP can be used in conjunction with a Tersoff potential for carbon.

The lattice parameter for c-BN is about 1.6% too small, which in general is not a problem. We note, however, that for applications to c-BN requiring a more accurate lattice parameter, the lattice parameter can be adjusted by a factor s_a without changing the binding energies by scaling the Tersoff parameters β and r_0 to $\tilde{\beta} = \beta/s_a$ and $\tilde{r}_0 = s_a r_0$, respectively, as can be shown analytically. Obviously, this scaling reduces the interatomic distances in all BN structures by the same factor, leading to a less accurate lattice parameter for h-BN, which, however, is irrelevant for applications to c-BN. It also changes the elastic moduli by a factor of the order of $1/s_a^2$, but as long as s_a is close to one, as it is the case here, these changes typically remain rather small.

The experimental bulk modulus of 3D h-BN is about one order of magnitude smaller than that for c-BN due to the high compressibility in the $c_\perp$ direction related to the relatively weak interactions between the h-BN layers. The bulk modulus B according to BN-ExTeP vanishes as it does not describe interlayer interactions. More relevant for us, however, are the in-plane or 2D elastic moduli B_{2D} and $C_{11,2D}$. For a strictly 2D, isotropic material these are related to the 2D shear modulus μ_{2D}, the 2D Young's modulus E_{2D}, and the in-plane Poisson's ratio ν_{2D} by the relations:

$$\mu_{2D} = C_{11,2D} - B_{2D}, \quad E_{2D} = \frac{4B_{2D}\mu_{2D}}{B_{2D}+\mu_{2D}} \quad \text{and}$$
$$\nu_{2D} = \frac{B_{2D}-\mu_{2D}}{B_{2D}+\mu_{2D}}, \tag{15}$$

respectively. Using these relations, we find a Poisson's ratio $\nu_{2D} \simeq 0.19$, which compares well to the *ab initio* value of 0.2 reported in Ref. [17]. In particular, the uniaxial elastic modulus of $C_{11} = 277$ N/m for h-BN is in much better agreement with the *ab initio* value than the too large value of $C_{11} = 396$ N/m according to the earlier Tersoff potential [7,16], that leads to a negative Poisson's ratio equal to $\nu = -0.17$ using the relations in Eq. (15).

Not shown in Table III is that BN-ExTeP also gives reasonable values for the lattice parameters and binding energies of the rock-salt and BCC structures. According to *ab initio* calculations [16] these unstable rock-salt and BCC BN compounds are about 3.5 and 7.8 eV/c.u. (eV per BN chemical unit) less stable than c-BN, respectively, while BN-ExTeP yields values of 3.88 and 9.33 eV, respectively, for these energy differences, the somewhat larger disagreement for the BCC BN compound being due to the effect of the cutoff. The lattice parameter of 3.535 Å for rock salt and 2.299 Å for the BCC BN compound according to BN-ExTeP correspond well to the DFT values of 3.474 Å and 2.32 Å, respectively.

The pure and compound systems considered in this section do not involve any nonzero correction term F_{IJ}. In fact, the correction terms $F_{BB}(0,0)$ and $F_{NN}(0,0)$ involved in the pure systems and the terms $F_{BN}(2,2)$ and $F_{BN}(3,3)$ involved in h-BN and c-BN, respectively, are all taken equal to zero. All other correction terms are adjusted to optimize the description of defects in h-BN and c-BN and of small BN clusters, as detailed in the next section.

B. Bond order correction

The correction term F_{ij} is a natural, first order correction to the bond order for binary systems, involving only nearest neighbors and their chemical identities. This term considerably improves the description of the formation energy and geometry (bond distances) of a whole series of defects and a number of small BN molecules. Clearly, this improvement comes at the cost of additional parameters, but it hardly affects the efficiency of the calculations, as it does not extend the environment involved in computing the bond order, which remains restricted to the nearest neighbors.

The correction term parameters are listed in Table IV. In Table V we describe the defects in h-BN and c-BN that we considered. For h-BN, these defects and selected bond lengths are illustrated in Fig. 1. The Stone-Wales (SW) defect in h-BN is the BN analog of the SW defect for graphene [39]. There are two local minima for the SW defect in h-BN, with different geometries around the defect as illustrated in the bottom panel of Fig. 1. As for graphene [40], the most stable structure is SW-1, a sinelike buckling around the defect. The antisite (AS) defect is created by swapping the chemical identity of

TABLE IV. Values of F_{IJ}. For integer arguments with $N_{ij}^{\bar{I}}$ or $N_{ji}^{\bar{J}} \geqslant 4$, F_{IJ} is zero.

	$N_{ij}^{\bar{B}} \backslash N_{ji}^{\bar{B}}$	0	1	2	3
	0	0.0000	0.0054	0.0182	−0.0034
F_{BB}	1	0.0054	0.0100	0.0062	0.0154
	2	0.0182	0.0062	0.0154	−0.0390
	3	−0.0034	0.0154	−0.0390	−0.1300
	$N_{ij}^{\bar{N}} \backslash N_{ji}^{\bar{N}}$	0	1	2	3
	0	0.0000	−0.0282	−0.0018	−0.0004
F_{NN}	1	−0.0282	0.0200	0.0180	0.0146
	2	−0.0018	0.0180	0.0306	0.0060
	3	−0.0004	0.0146	0.0060	0.0000
	$N_{ij}^{\bar{B}} \backslash N_{ji}^{\bar{N}}$	0	1	2	3
	0	0.0170	0.0078	0.0000	−0.0860
F_{BN}	1	−0.0090	0.0090	−0.0068	−0.0338
	2	0.0000	−0.0198	0.0000	−0.0084
	3	−0.0750	−0.0168	−0.0138	0.0000

TABLE V. Considered defects in h-BN and c-BN with involved correction terms F_{IJ}. Formation energies E_f in eV as found with the classical potentials of Albe and Möller [7], Kınacı *et al.* [10], and from this work are compared to DFT calculations with DMol from Ref. [16] and those calculated using SIESTA by us.

		E_f (Classical Potentials)			E_f (DFT)	
***h*-BN**	F_{IJ} involved	[7]	[10]	BN-ExTeP	[16]	SIESTA
AS	$F_{BB}(1,2)$, $F_{NN}(1,2)$, $F_{BN}(1,2)$, $F_{BN}(2,1)$	7.3	9.3	8.1	8.1	8.52
SW-1	$F_{BB}(2,2)$, $F_{NN}(2,2)$, $F_{BN}(1,1)$, $F_{BN}(1,2)$, $F_{BN}(2,1)$	9.18	6.44	7.22		7.20
SW-2	$F_{BB}(2,2)$, $F_{NN}(2,2)$, $F_{BN}(1,1)$, $F_{BN}(1,2)$, $F_{BN}(2,1)$	9.12	6.74	7.43		7.34
B sub	$F_{BB}(0,2)$, $F_{BN}(1,2)$	5.0	6.8	5.7	5.7	6.50
N sub	$F_{NN}(0,2)$, $F_{BN}(2,1)$	5.8	7.1	9.1	9.1	8.98
B vac	$F_{BN}(2,1)$	4.7	4.7	10.4	10.4	10.55
N vac	$F_{BN}(1,2)$	5.6	5.6	7.3	7.3	6.25
Interc. B1	$F_{BB}(1,3)$, $F_{BN}(2,3)$	3.4	3.6	7.3	7.3	
Interc. B2	$F_{BB}(2,3)$, $F_{BN}(1,3)$, $F_{BB}(2,3)$	4.3	5.6	8.0	–	
Interc. N1	$F_{NN}(1,3)$, $F_{BN}(3,2)$	3.5	3.3	6.6	–	
Interc. N2	$F_{NN}(2,3)$, $F_{BN}(3,1)$, $F_{BN}(3,2)$	3.2	0.5	7.3	7.3	
***c*-BN**						
AS	$F_{BB}(1,3)$, $F_{NN}(1,3)$, $F_{BN}(2,3)$, $F_{BN}(3,2)$	7.0	10.2	9.1	9.1	
B sub	$F_{BB}(0,3)$, $F_{BN}(2,3)$	2.1	5.5	9.1	9.1	
N sub	$F_{NN}(0,3)$, $F_{BN}(3,2)$	5.8	9.3	10.2	10.2	
B vac	$F_{BN}(3,2)$	3.4	2.6	9.2	9.2	
N vac	$F_{BN}(2,3)$	2.5	3.5	7.3	7.3	

two nearest neighbor atoms. The B (N) substitutional defects are created replacing an individual N (B) atom by B (N). The intercalation defects are created by putting an additional atom between two layers of h-BN in AA stacking, where N atoms of the first layer are above B in the second. The intercalated atom is then chemically bound to both layers, being either vertically intercalated between B and N (B1 or N1), or diagonally between two atoms with chemical identities different from itself (B2 or N2).

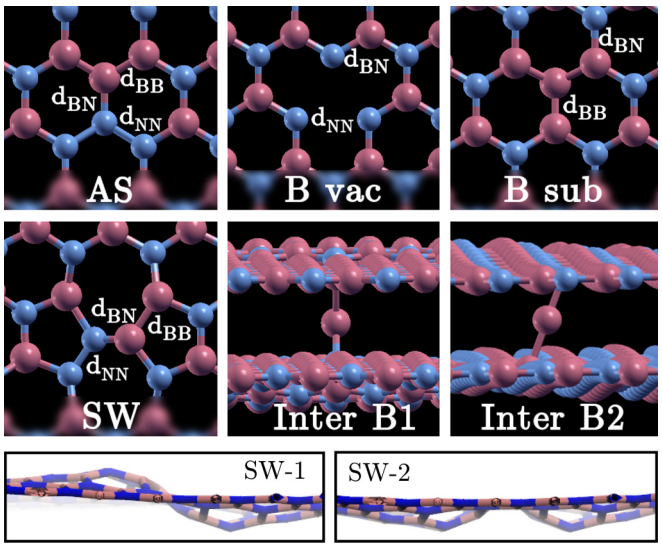

FIG. 1. Point defects in h-BN and distances considered in Table VI. For the Stone-Wales defect side views of the antisymmetric (SW-1) and symmetric (SW-2) realizations are shown in the bottom panel.

The defect formation energies E_f of our neutral defects are calculated as [16,41,42]:

$$E_f = E_D - n_B\mu_B^{BN} - n_N\mu_N^{BN}, \tag{16}$$

where E_D is the total energy of the defected system, n_B and n_N are the number of B and N atoms in the supercell, respectively, and μ_B^{BN} and μ_N^{BN} their chemical potentials in the BN compound phase. Following Ref. [16], Eq. (16) can be rewritten to:

$$E_f = E_D - \tfrac{1}{2}(n_B + n_N)\mu_{BN} - \tfrac{1}{2}(n_B - n_N)(\mu_B - \mu_N), \tag{17}$$

where $\mu_{BN} = \mu_B^{BN} + \mu_N^{BN} = \mu_B + \mu_N + \Delta H_f$ is the chemical potential per BN pair in the compound bulk phase, μ_B and μ_N are the chemical potentials of B and N in pure component reference phases, and ΔH_f is the formation enthalpy. In the present case, μ_{BN} is just the ground state binding energy, equal to -13.38 and -13.49 eV/c.u. for h-BN and c-BN, respectively, according to BN-ExTeP (see Table III). Obviously, for the calculation of the *ab initio* formation energies, the respective *ab initio* ground state binding energies were used. It can be shown that, in thermodynamic equilibrium, $\mu_B - \mu_N$ is approximately equal to the difference in the binding energy per atom of the pure component reference phases. We have chosen the reference phases to be solid α phase for boron and diatomic N_2 for nitrogen, with binding energies 5.81 and 4.92 eV/atom, respectively, yielding $\mu_B - \mu_N = -0.89$ eV/atom in thermodynamic equilibrium.

Each defect involves one or more correction term values for integer arguments, specified in the second column of Table V, which are adjusted to optimize the defect description. The resulting defect formation energies for optimized geometries in Table V are globally in very good agreement with those from DFT calculations [16] and significantly improve the formation energies with respect to previous potentials from

TABLE VI. Interatomic distances for defects in h-BN, compared to *ab initio* values calculated using the SIESTA code.

Structure	d_{BB} (Å)	d_{NN} (Å)	d_{BN} (Å)
AS	1.60 (1.61)	1.44 (1.44)	1.36 (1.36)
SW-1	1.60 (1.68)	1.41 (1.46)	1.37 (1.36)
SW-2	1.60 (1.68)	1.40 (1.46)	1.37 (1.35)
B sub	1.55 (1.63)		1.47 (1.45)
N sub		1.53 (1.49)	1.51 (1.44)
B vac		2.60 (2.58)	1.48 (1.40)
N vac	2.66 (2.27)		1.43 (1.47)

Refs. [7,10] listed in the same table. They are all in the right order, with most of the defects in h-BN having formation energies between 5 and 10 eV and the B substitutional defect having the lowest formation energy. There is a small energy difference between the two SW defects, assigning the correct most stable configuration when compared to the *ab initio* calculations. BB-ExTeP predicts higher stability of the B1 and N1 intercalation defects compared to the B2 and N2 types, respectively. For the B interaction this seems in agreement with *ab initio* calculations but not for the N intercalation. We note that the formation energy of the B2 and N1 intercalation defects could not be determined in the DMol calculations as they transformed into the more stable B1 and N2 structures, respectively, during geometrical optimization.

Experimentally observed vacancy defects, created by an electron beam, have been associated with only one of the two sublattices [13], which was later identified as a predominance of B monovacancies [43]. This is in contrast with its higher formation energy (Table V). It should be noticed, however, that although the formation energy provides a valuable tool in the construction of a potential and the comparison of theoretical methods, it is a difficult quantity to relate directly to experiments as its value depends on the chosen reference states, that may not reflect the experimental environment, and does not consider kinetic effects nor the dynamical stability, determined, e.g., by energies barriers. In the present case, the abundance of B monovacancies may be due to the lighter mass of B, making it more easy to excite B atoms to a state where they have a velocity large enough for escape from the lattice.

Bond distances around a number of important defects in h-BN are given in Table VI and compared to the values in parenthesis from *ab initio* calculations using the SIESTA code. Differences with *ab initio* values are relatively small and not larger than 5% in all cases except for the N vacancy, which is overall satisfactory.

Apart from the defects, also linear and triangular B_2N and BN_2 clusters were used as references for the adjustment of a number of correction terms F_{ij}. These are listed in Table VII, together with their binding energy per atom E_b and bond distances after geometrical optimization, compared to the DMol results. The table shows that the binding energies for these small binary clusters are substantially smaller that those in the stable compound bulk phases, implying that such clusters are relatively unstable in a BN environment, which is correctly reproduced by the classical potential. Therefore, trying to reduce the somewhat larger disagreements with the DMol values for the triangular clusters was not given a high priority.

TABLE VII. Linear and triangular three atom binary B-N clusters considered for adjustment of the specified correction terms F_{IJ}, their binding per atom and associated bond distances, compared to the DMol values [16] in parenthesis.

Structure	F_{ij}	E_b (eV/atom)	d_{IJ} (Å)
lin. BBN	$F_{BB}(1,0)$	3.31 (3.32)	$d_{BB} = 1.59$ (1.55)
	$F_{BN}(0,0)$		$d_{BN} = 1.30$ (1.31)
lin. BNB	$F_{BN}(0,1)$	4.09 (4.10)	$d_{BN} = 1.34$ (1.32)
tr. B_2N	$F_{BB}(1,1)$	3.42 (3.93)	$d_{BB} = 1.60$ (1.68)
	$F_{BN}(0,1)$		$d_{BN} = 1.62$ (1.35)
lin. BNN	$F_{NN}(1,0)$	3.52 (3.52)	$d_{NN} = 1.45$ (1.19)
	$F_{BN}(0,0)$		$d_{BN} = 1.30$ (1.33)
lin. NBN	$F_{BN}(1,0)$	3.37 (3.37)	$d_{BN} = 1.40$ (1.36)
tr. BN_2	$F_{NN}(1,1)$	2.44 (3.56)	$d_{NN} = 1.74$ (1.34)
	$F_{BN}(1,0)$		$d_{BN} = 1.46$ (1.43)

We note that the h-BN nanoribbon edge formation energies are also reasonably well reproduced without being considered during the parametrization. We find formation energies of 9.0 and 12.2 eV/nm for the armchair and zigzag edges of h-BN, respectively, compared to DFT-PBE values of 7.6 and 11.2 eV/nm [44].

IV. APPLICATION TO PRISTINE h-BN

To introduce the study of the elastic moduli of defective h-BN presented in the next section, we first comment on some basic properties of pristine h-BN as obtained by molecular dynamics (MD) simulations with BN-ExTeP. Some of these properties were also investigated in a previous study [45,46] based on an earlier BN Tersoff potential [7].

For this and the following section we performed a series of classical molecular dynamics simulations at constant temperature and constant-pressure (NPT). The equations of motion including thermostat and barostat [47] are integrated with a timestep of 1 fs. For both the Nosé-Hoover thermostat and barostat, we used a coupling constant (damping parameter) of 1 ps. The barostat is only applied to the in-plane dimensions of the membrane. We consider a sheet of h-BN consisting of 37 888 atoms in a periodic cell of $L_x \times L_y = 32.4 \times 32.6$ nm^2 (74×128 orthorhombic unit cells). The x and y directions here correspond to zigzag and armchair axes, respectively. The perpendicular cell size ($L_z = 4$ nm) is large enough to avoid interaction between periodic images of the sheet.

We first examine the temperature dependence of the 2D lattice parameter. For this, we performed 48 independent MD simulations at temperatures up to 4000 K. Each of these simulations ran for 200 ps of which the last 100 ps were used to obtain average lattice constants. The result is shown in the top panel of Fig. 2. The decrease of the lattice parameter is a consequence of thermal rippling. Unlike the situation for graphene, however, for which a minimum in a corresponding to a compression of $\sim$0.2% was found at 900 K [48] from simulations based on the carbon potential LCBOPII [49], here a does not have a minimum but decreases monotonously up to a temperature close to or beyond the melting temperature, where a compression of about 1% is reached. This behavior also deviates from the results for h-BN in Ref. [45] by

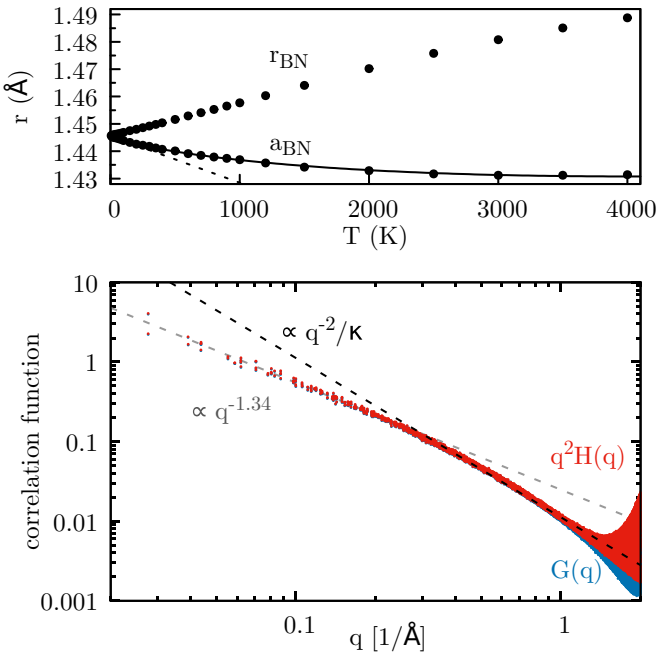

FIG. 2. (top) Average in-plane lattice parameter $a_{BN} = (a/a_0)r_{NB,0}$ and average B-N nearest neighbor distance r_{NB} as a function of temperature, with $r_{NB,0}$ the nearest neighbor distance at $T = 0$ K and $a_0 = 2.504$ Å the ground state lattice parameter. The dashed line is a linear fit up to 100 K, $a = a_0(1 + \alpha T)$ with $\alpha = -1.181\times10^{-5}$ K^{-1}. A good fit over the whole range (solid line) is found with the form $a = a_0(1 + \alpha_1 T + (\alpha_2 T)^{\xi})$, with $\alpha_1 = 5.16\times10^{-4}$ K^{-1}, $\alpha_2 = 5.204\times10^{-4}$, and $\xi = 0.995$. (bottom) Normal-normal [G(q)] and height-height [$q^2H(q)$] correlation functions at room temperature $T = 300$ K. The harmonic regime $\propto q^{-2}$ (dashed line) yields a bending rigidity $\kappa = 0.85$ eV. For $q \to 0$ we find a power law with exponent $-(2 - \eta)$ with $\eta \sim 0.66$.

simulations based on the earlier BN potential by Albe [7] and in Ref. [50] based on the potential of Kinaci [10]. In these previous studies, minima in a were found at 1500 K and 2000 K, respectively, corresponding to a compression of about 0.5% in both cases. A negative thermal expansion coefficient is a common property of all membranes in the quasiharmonic approximation [51]; it follows from negative (and divergent at small wave vectors) microscopic Grüneisen parameters for the acoustic flexural mode [52] and has also been measured experimentally for graphene [53]. The change of its sign at high enough temperatures, which is also predicted for graphene [48], is an anharmonic effect beyond the quasiharmonic approximation and beyond the macroscopic phenomenological theory of membranes, namely it is determined by phonon-phonon interactions over the whole Brillouin zone [54]. The temperature at which this change in sign appears, however, can be higher than the melting temperature, as seems to be the case for h-BN according to BN-ExTeP.

In contrast to the 2D lattice parameter, which decreases, the B-N nearest neighbor distance monotonously increases with temperature, as also shown in Fig. 2. This expected, approximately linear increase was also noticed for graphene in Ref. [55].

We also considered the structure of the thermal rippling at $T = 300$ K. For this we did a separate MD simulation of 1.25 ns, of which an initial part was used for thermalization and the remaining part for averaging. From these simulations we computed the Fourier transform of the normal-normal correlation function, $G(q) = \langle|\mathbf{n}_q|^2\rangle = N^{-1}\langle|\sum_i^N \hat{\mathbf{n}}_i \exp(i\mathbf{q}\mathbf{r}_{i,0})|^2\rangle$ and height-height correlation function $H(q) = \langle|h_q|^2\rangle = N^{-1}\langle|\sum_i^N h_i \exp(i\mathbf{q}\mathbf{r}_{i,0})|^2\rangle$ with $\hat{\mathbf{n}}_i$ the unit vector normal to the surface at site i, h_i the height at site i, $\mathbf{q}$ the wave vector in Fourier space, and $\{\mathbf{r}_{i,0}\}$ the ground state atomic positions. These were calculated as done for graphene in Ref. [56] and are shown in the bottom panel of Fig. 2. It holds that $G(q) = q^2H(q)$. In the harmonic approximation, i.e., for large q (roughly from 0.3 to 1 Å^{-1} in the present case), we have $H(q) = \rho k_B T/(\kappa q^4)$ and $G(q) = \rho k_B T/(\kappa q^2)$, with ρ the 2D density in atoms/Å^2 and κ the bending rigidity. With this we find $\kappa = 0.85$ eV compared to 0.96 eV from *ab initio* calculations [57] and 0.86–1 eV as calculated using the potential by Kınacı *et al.* [10] in Ref. [58]. According to these results, freestanding h-BN is about as rigid as freestanding graphene, for which a bending rigidity of $\kappa = 1.1$ eV was found at $T = 300$ K [59] using the LCBOPII interatomic potential for carbon [49], the latter value being slightly smaller than $\kappa = 1.2$ eV obtained experimentally via the phonon spectrum of graphite [60].

In the long wavelength limit, due to strong anharmonic coupling between in-plane modes and out-of-plane flexural modes, height fluctuations are suppressed and the correlation function behaves as $G(q) = \propto q^{2-\eta}$, with η a nontrivial critical exponent. From our calculated $G(q)$ we find $\eta \sim 0.66$, compared to 0.85 found for graphene [56]. While this difference may appear to be significant, it should be noted that the value of η obtained from simulations can depend on simulation settings and tends to converge very slowly. We estimate the error in our extracted exponent to be approximately of the order of this difference, so that the supposed universality of this behavior is neither contradicted nor confirmed.

We investigated the elastic behavior of pristine h-BN under uniaxial strain by running simulations at a temperature T near 0 K. The results are summarized in Fig. 3 and allow us to recalculate the elastic modulus and Poisson's ratio independently and verify the consistency of Eq. (15) in this way. Note that the E_{2D} and ν in Table III were calculated from B_{2D} and C_{11} using Eq. (15). The top-left figure shows the applied, fixed L_x and free L_y cell size dimensions. The sample used in this simulation is initially compressed to 99.5% of its equilibrium value along the x direction. After 2 ns equilibration, the sample is then gradually extended to 100.5% during 10 ns MD in steps of 0.1%. The cell size in the y direction is kept free and is found to decrease, indicating a positive Poisson's ratio equal to 0.19 in agreement with the value in Table III.

In the bottom-left panel of Fig. 3, the stress component in the x direction, σ_{xx}, as a function of simulation time is shown. On the right-hand side, time averages of the energy and stress as a function of the fixed strain are shown. For compressive strain, σ_{xx} remains very small as a result of induced static corrugation. The same can be seen from the energy increase at negative strain (top-right panel), which is evidently not quadratic, as for positive (tensile) strain, but displays a much smaller, near-constant increase in average

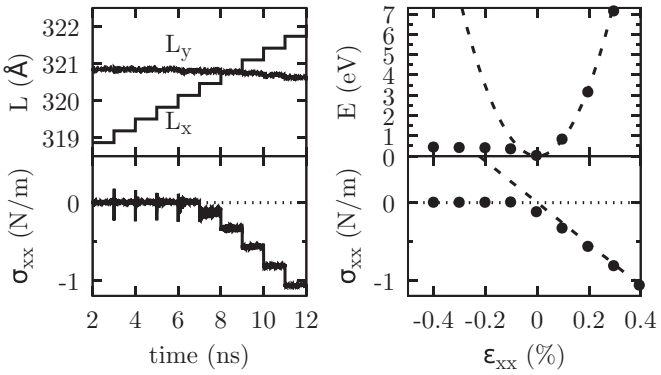

FIG. 3. Summary of the results from simulations of pristine h-BN under uniaxial applied strain ϵ_{xx} in the x direction, varied in steps from 0.95 to 1.05 as described in the text, at a temperature near 0 K with size fluctuations in the y direction. The top left panel shows how L_x is varied in steps to induce the strain and the monitored L_y during the simulation. The bottom left panel shows the monitored xx component of the stress tensor σ_{xx}. The right panels show the average energy per atom (top) and the average σ_{xx} as a function of the applied strain ϵ_{xx}. The dashed line in the right top panel corresponds to a $E_{2D} = 267$ N/m.

potential energy illustrative of strong anharmonicity. The simulation data for positive strain part ($\epsilon_{xx} > 0$) are very well fitted by the quadratic curve (dashed line) yielding a the 2D Young's modulus of $E_{2D} = 267$ N/m, consistent with Table III.

V. APPLICATION TO DEFECTIVE h-BN

To study the effect of defects on the elastic properties of h-BN, we consider six defect types. These are the Stone-Wales (SW) and antisite (AS) defects, vacancies (B and N) and substitutional defects (B and N). Here we notice that the results presented in this section have been obtained from a slightly different parametrization of our potential [61]. This does not change qualitatively the results and has a negligible quantitative effect as we verified.

We use the same sample size as considered for pristine h-BN in the preceding section. For each defect type we then consider seven defect densities up to 0.7 nm^{-2} corresponding to 38, 76, 114, 152, 228, 304, and 760 defects and for each of these densities we consider between five and eight different randomly generated defect distributions. For each of these samples we then first perform a thermal optimization. To subsequently determine the elastic moduli, we used the same procedure as described earlier for pristine h-BN.

Our thermal optimization procedure is done in the NPT ensemble at $P = 0$ and consists of a 200 ps heating from 100 to 1000 K, thermalization at 1000 K for 2 ns, cooling down to 10 K in 300 ps, followed by a conjugate gradient minimization. The final structures gives us the equilibrium lattice parameters and the defect formation energies including defect-defect interactions.

The results are shown in Fig. 4. The panels in the first row show the relative cell sizes in the x direction for the optimized structures. All defects considered here result in a

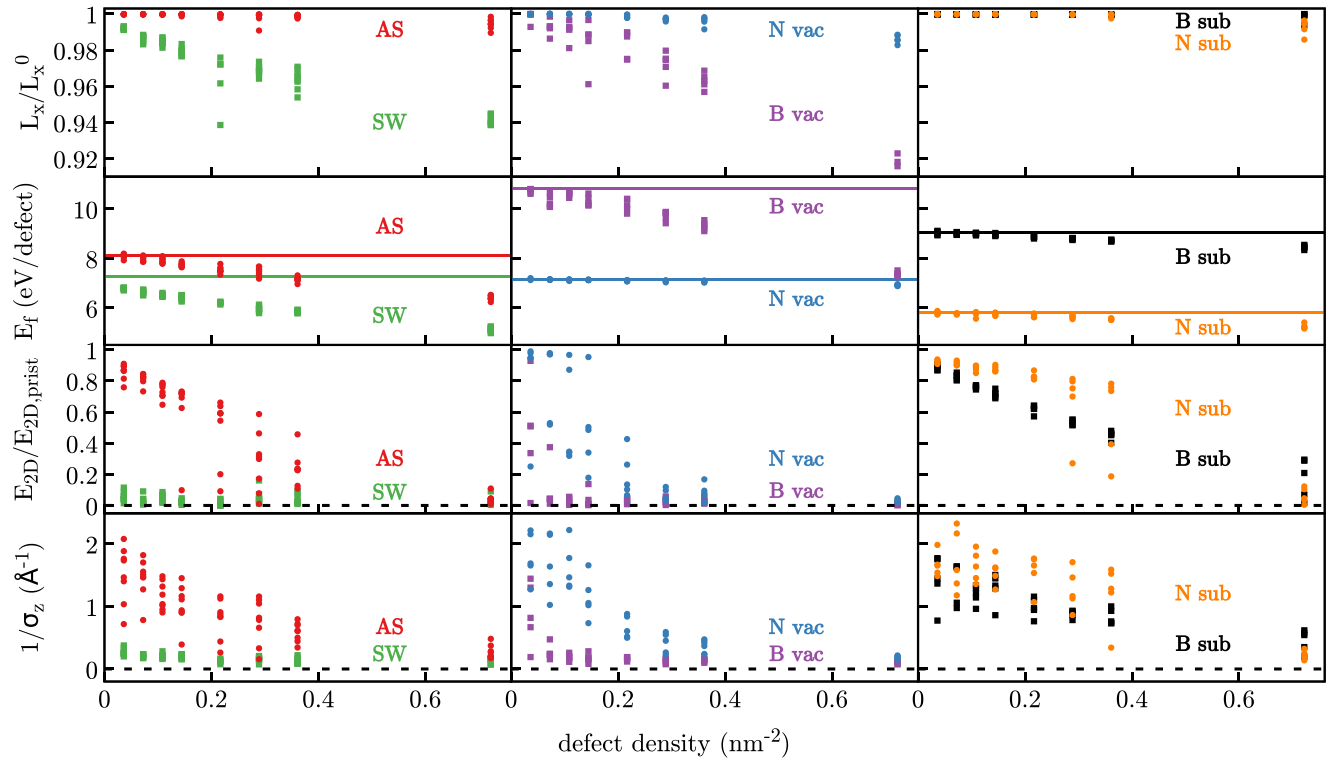

FIG. 4. From top to bottom, rows of panels show the static strain L_x/L_x^0, average defect formation energies E_f, relative elastic moduli $E_{2D}/E_{2D,\text{prist}}$, and inverse corrugation $1/\sigma_z$, with σ_z the average height fluctuation of the annealed samples, as a function of the defect concentration. Multiple symbols are results for different random realizations. Defect types are as indicated in the graph. In the plots of the E_f, horizontal lines indicate the isolated defect formation energy for reference.

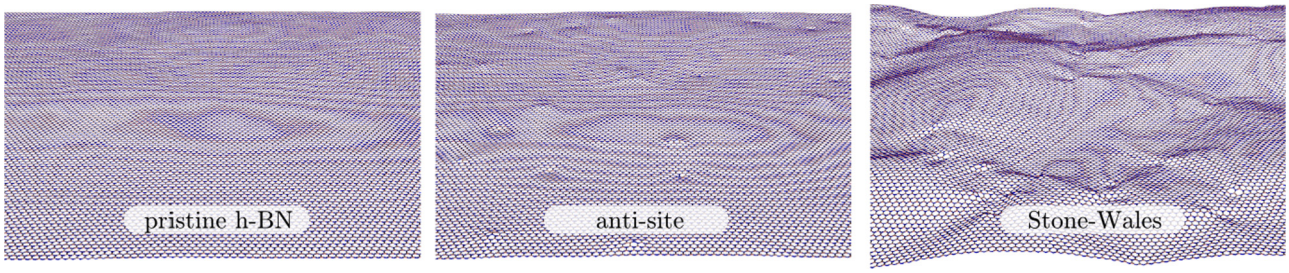

FIG. 5. Illustration of selected structures at $T = 0$ K. The AS and SW defect densities (middle and right panel) are 0.036 nm^{-2}, the lowest defect densities considered here.

decrease of the cell size with respect to pristine h-BN. SW defects and B vacancies show the most obvious decrease, being roughly linear as a function of the defect density. This can be understood as a result of static corrugation. Contrary to thermal rippling, static corrugation does not disappear at low temperatures because it is the result of local curvature induced by the defects. These out-of-plane distortions lead to a reduction of the in-plane lattice constant. As an example, the optimized structure of pristine h-BN is compared to those of h-BN with AS and SW defects in Fig. 5. The pristine lattice is entirely flat in the low temperature limit. Antisite defects induce small localized distortions while Stone-Wales defects lead to much stronger and longer-ranged distortions. As a result, the samples with SW defects are indeed strongly corrugated and their associated cell sizes are significantly reduced. Substitutional defects present very little corrugation and correspondingly have nearly unchanged lattice constants.

The second row of Fig. 4 shows the corresponding defect formation energies (in eV per defect). Note that, while all are drawn on the same scale, the absolute values of formation energies depend on the conventions used for Eqs. (16) and (17), related to the choice of the pure component reference systems. The SW defects and B vacancies, as well as the AS defects, show a strong linear decrease in formation energy as a function of defect density. This indicates that defects that induce strong corrugation highly prefer being in close proximity over being far apart, a behavior also observed for graphene [62,63]. On the contrary, N vacancies and substitutional defects appear to interact only weakly and thus do not significantly affect formation energies. Only at elevated defect densities a small energy gain can be noticed for the vacancy configurations, which is mostly the result of reconstructions during the annealing procedure.

The third row of Fig. 4 shows the calculated Young's moduli relative to the value for pristine h-BN. In all cases E_{2D} is significantly affected by the defects, albeit in qualitatively different ways. SW defects and B vacancies dramatically decrease the Young's modulus, even at low concentrations. Also this can be understood from the corrugation of the sample. When the corrugated sample is stretched, the energy required to flatten the system is much smaller than if chemical bonds were to be stretched directly as in the case of (flat) pristine h-BN. The AS and substitutional vacancies lead to a much more gradual and approximately linear decrease in elastic moduli. Finally, N vacancies show again a different behavior. At low densities their elastic moduli are nearly unaffected, but as the concentration increases, defect reconstructions start to occur and the elastic moduli suddenly drop similar to what was observed for SW defects and B vacancies despite being accompanied by a rather small change in average cell size. For vacancies in graphene, the Young's modulus has been observed to increase at concentrations below $\sim$0.1 nm^{-1} (0.2%) [64]. Such an increase in E_{2D} can be the result of pre-straining created during the formation of vacancies, which suppresses anharmonic effects and by this the impact of anharmonicity on the effective elastic modulus [65] assuming a clamped boundary of the system. Our samples are not pre-strained because our simulations are at zero pressure and anharmonic effects due to thermal height fluctuations do not play a role at $T = 0$ K.

To illustrate the strong correlation between the behavior of the elastic moduli and the static corrugation more explicitly, we have calculated the average height fluctuation, $\sigma_z^2 = \langle (z - \langle z \rangle)^2 \rangle$, which is shown in the last row of Fig. 4. Indeed, we find that the values for σ_z vary similarly with defect concentration as the elastic moduli, consistent with the foregoing discussion.

VI. CONCLUSIONS AND PERSPECTIVES

We have developed BN-ExTeP, an extended Tersoff potential for B, N, and BN describing a wide range of structures and being particularly accurate for the description of defects in h-BN and c-BN. The potential can be used efficiently to study the statistical mechanics of large (defected) h-BN sheets, knowing that large system size is very important for 2D systems. BN-ExTeP can also be a valuable tool for large-scale simulations involving chemical reactions and phase transformations, such as the melting and growth of h-BN or c-BN, as it correctly describes the bonding trends in BN systems.

Having demonstrated that the ExTeP scheme proposed here for BN systems can provide a significant improvement in the accuracy of bonding as a function of chemical environment, we believe that the here proposed correction term is a good candidate, not only to correct other Tersoff potential parametrizations for BN but for other binary systems as well. Moreover, this approach has the important quality of hardly affecting the efficiency of the computations with respect to the original Tersoff potential scheme.

We have implemented BN-ExTeP in LAMMPS and used this classical potential to study the effect of defects on the elastic properties of h-BN. We find that the calculated weakening of the elastic moduli parallels the defect-induced growth of static corrugation.

ACKNOWLEDGMENTS

The research leading to these results received funding from the Foundation for Fundamental Research on Matter (FOM), part of the Netherlands Organisation for Scientific Research (NWO). The work was carried out on the Dutch national e-infrastructure with the support of SURF Cooperative. This project has received funding from the European Union's Horizon 2020 research and innovation programme under Grant Agreement No. 696656 – GrapheneCore1. We thank P. G. Steeneken and G. Slotman for useful comments and A. Loiseau and C. Bichara for supporting this project.

[1] A. K. Geim and I. V. Grigorieva, Nature (London) **499**, 419 (2013).
[2] C. R. Dean, A. F. Young, I. Meric, C. Lee, L. Wang, S. Sorgenfrei, K. Watanabe, T. Taniguchi, P. Kim, K. L. Shepard, and J. Hone, Nat. Nanotechnol. **5**, 722 (2010).
[3] L. Britnell, R. V. Gorbachev, R. Jalil, B. D. Belle, F. Schedin, A. Mishchenko, T. Georgiou, M. I. Katsnelson, L. Eaves, S. V. Morozov, N. M. R. Peres, J. Leist, A. K. Geim, K. S. Novoselov, and L. A. Ponomarenko, Science **335**, 947 (2012).
[4] K. Watanabe, T. Taniguchi, and H. Kanda, Nat. Mater **3**, 404 (2004).
[5] L. Schué, B. Berini, A. C. Betz, B. Plaçais, F. Ducastelle, J. Barjon, and A. Loiseau, Nanoscale **8**, 6986 (2016).
[6] R. Bourrellier, S. Meuret, A. Tararan, O. Stéphan, M. Kociak, L. H. G. Tizei, and A. Zobelli, Nano Lett. **16**, 4317 (2016).
[7] K. Albe and W. Möller, Comput. Mater. Sci. **10**, 111 (1998).
[8] K. Matsunaga, C. Fisher, and H. Matsubara, Jpn. J. Appl. Phys. **39**, L48 (2000).
[9] C. Sevik, A. Kinaci, J. B. Haskins, and T. Çağın, Phys. Rev. B **84**, 085409 (2011).
[10] A. Kınacı, J. B. Haskins, C. Sevik, and T. Çağın, Phys. Rev. B **86**, 115410 (2012).
[11] M. R. Weismiller, A. C. T. van Duin, J. Lee, and R. A. Yetter, J. Phys. Chem. A **114**, 5485 (2010).
[12] S. J. Pai, B. C. Yeo, and S. S. Han, Phys. Chem. Chem. Phys. **18**, 1818 (2016).
[13] J. C. Meyer, A. Chuvilin, G. Algara-Siller, J. Biskupek, and U. Kaiser, Nano Lett. **9**, 2683 (2009).
[14] C. Jin, F. Lin, K. Suenaga, and S. Iijima, Phys. Rev. Lett. **102**, 195505 (2009).
[15] T. Pham, A. L. Gibb, Z. Li, S. M. Gilbert, C. Song, S. G. Louie, and A. Zettl, Nano Lett. **16**, 7142 (2016).
[16] K. Albe, Computersimulationen zu Struktur und Wachstum von Bornitrid, Ph.D. thesis, Technische Universität Dresden, http://nbn-resolving.de/urn:nbn:de:bsz:d120-qucosa-30654 (1998).
[17] K. N. Kudin, G. E. Scuseria, and B. I. Yakobson, Phys. Rev. B **64**, 235406 (2001).
[18] D. Sánchez-Portal and E. Hernández, Phys. Rev B **66**, 235415 (2002).
[19] S. J. Plimpton, J. Comput. Phys. **117**, 1 (1995).
[20] J. Tersoff, Phys. Rev. Lett. **56**, 632 (1986); **61**, 2879 (1988); Phys. Rev. B **38**, 9902 (1988); **37**, 6991 (1988).
[21] J. H. Los and A. Fasolino, Phys. Rev. B **68**, 024107 (2003).
[22] J. M. Soler, E. Artacho, J. D. Gale, A. García, J. Junquera, P. Ordejón, and D. Sánchez-Portal, J. Phys.: Condens. Matter **14**, 2745 (2002).
[23] J. P. Perdew, Phys. Rev. B **33**, 8822 (1986); **34**, 7406 (1986).
[24] N. Troullier and J. L. Martins, Phys. Rev. B **43**, 1993 (1991).
[25] N. N. Greenwood, *Boron* (Pergamon Press, Lincoln, UK, 1975).
[26] J. Widany, T. Frauenheim, T. Köhler, M. Sternberg, D. Porezag, G. Jungnickel, and G. Seifert, Phys. Rev. B **53**, 4443 (1996).
[27] M. M. van Wijk, A. Schuring, M. I. Katsnelson, and A. Fasolino, Phys. Rev. Lett. **113**, 135504 (2014).
[28] R. Wycko, *Crystal Structures* (Interscience Publishers, New York, 1974).
[29] C. Kittel, *Introduction to Solid State Physics*, 8th ed. (Wiley, Hoboken, NJ, 2005).
[30] V. L. Solozhenko, G. Will, and F. Elf, Solid State Commun. **96**, 1 (1995).
[31] R. W. Lynch and H. G. Drickamer, J. Chem. Phys. **44**, 181 (1966).
[32] A. Bosak, J. Serrano, M. Krisch, K. Watanabe, T. Taniguchi, and H. Kanda, Phys. Rev. B **73**, 041402 (2006).
[33] N. Ohba, K. Miwa, N. Nagasako, and A. Fukumoto, Phys. Rev. B **63**, 115207 (2001).
[34] Q. Peng, Wei Ji, and Suvranu De, Computat. Mater. Sci. **56**, 11 (2012).
[35] H. Neumann, Cryst. Res. Technol. **30**, 910 (1995).
[36] E. Knittle, R. M. Wentzcovitch, R. Jeanloz, and M. L. Cohen, Nature (London) **337**, 349 (1989).
[37] T. Sōma, A. Sawaoka, and S. Saito, Mater. Res. Bull. **9**, 755 (1974).
[38] M. Grimsditch, E. S. Zouboulis, and A. Polian, J. Appl. Phys. **76**, 832 (1994).
[39] A. J. Stone and D. J. Wales, Chem. Phys. Lett. **128**, 501 (1986).
[40] J. Ma, D. Alfè, A. Michaelides, and E. Wang, Phys. Rev. B **80**, 033407 (2009).
[41] S. Okada, Phys. Rev. B **80**, 161404 (2009).
[42] W. Orellana and H. Chacham, Phys. Rev. B **63**, 125205 (2001).
[43] K. Suenaga, H. Kobayashi, and M. Koshino, Phys. Rev. Lett. **108**, 075501 (2012).
[44] R. Mukherjee and S. Bhowmick, J. Chem. Theory Comput. **7**, 720 (2011).
[45] G. J. Slotman and A. Fasolino, J. Phys.: Condens. Matter **25**, 045009 (2013).
[46] During the present study we have realized that the results reported in Ref. [45] for defective structures are flawed by an error in the Tersoff parameters whereas they are correct for pristine *h*-BN.
[47] W. Shinoda, M. Shiga, and M. Mikami, Phys. Rev. B **69**, 134103 (2004).
[48] K. V. Zakharchenko, M. I. Katsnelson, and A. Fasolino, Phys. Rev. Lett. **102**, 046808 (2009).
[49] J. H. Los, L. M. Ghiringhelli, E. J. Meijer, and A. Fasolino, Phys. Rev. B **72**, 214102 (2005).
[50] S. Thomas, K. M. Ajith, S. Chandra, and M. C. Valsakumar, J. Phys.: Condens. Matter **27**, 315302 (2015).
[51] N. Mounet and N. Marzari, Phys. Rev. B **71**, 205214 (2005).

[52] P. L. de Andres, F. Guinea, and M. I. Katsnelson, Phys. Rev. B **86**, 144103 (2012).
[53] D. Yoon, Y.-W. Son, and H. Cheong, Nano Lett. **11**, 3227 (2011).
[54] M. I. Katsnelson and A. Fasolino, Acc. Chem. Res. **46**, 97 (2013).
[55] M. Pozzo, D. Alfè, P. Lacovig, P. Hofmann, S. Lizzit, and A. Baraldi, Phys. Rev. Lett. **106**, 135501 (2011).
[56] J. H. Los, M. I. Katsnelson, O. V. Yazyev, K. V. Zakharchenko, and A. Fasolino, Phys. Rev. B **80**, 121405 (2009).
[57] J. M. H. Kroes, A. Fasolino, and M. I. Katsnelson, Phys. Chem. Chem. Phys. **18**, 19359 (2016).
[58] S. K. Singh, M. Neek-Amal, S. Costamagna, and F. M. Peeters, Phys. Rev. B **87**, 184106 (2013).
[59] A. Fasolino, J. H. Los, and M. I. Katsnelson, Nat. Mater. **6**, 858 (2007).
[60] R. Nicklow, N. Wakabayashi, and H. G. Smith, Phys. Rev. B **5**, 4951 (1972).
[61] After peer review several modifications were made in the parametrization of BN-ExTeP to improve the description of pristine h-BN and c-BN and their melting behavior. These modifications did not affect the quality of the description of defective structures. In view of the considerable computational effort for the large amount of simulations performed for Sec. V, it was not possible to repeat them all. Therefore we repeated only part of the simulations with the final parametrization given in this paper and verified that the results are not affected.
[62] J. H. Los, K. V. Zakharchenko, M. I. Katsnelson, and A. Fasolino, Phys. Rev. B **91**, 045415 (2015).
[63] J. M. Carlsson, L. M. Ghiringhelli, and A. Fasolino, Phys. Rev. B **84**, 165423 (2011).
[64] G. López-Polín, C. Gómez-Navarro, V. Parente, F. Guinea, M. I. Katsnelson, F. Pérez-Murano, and J. Gómez-Herrero, Nat. Phys. **11**, 26 (2015).
[65] J. H. Los, A. Fasolino, and M. I. Katsnelson, Phys. Rev. Lett. **116**, 015901 (2016).